

PFC/JA-95-36

**Chaotic Behavior and Halo Development
in the Transverse Dynamics
of Heavy Ion Beams**

C. Chen, Qian Qian,* Ronald C. Davidson*

September 1995

MIT Plasma Fusion Center
Cambridge, Massachusetts 02139 USA

*Princeton Plasma Physics Laboratory, Princeton University, Princeton, NJ 08543

This work was supported in part by the US Department of Energy under Contract No. DE-AC02-76-CHO-3073, and in part by the Office of Naval Research. Reproduction, translation, publication, use, and disposal, in whole or in part, by or for the US Government is permitted.

Submitted for publication in: Fusion Engineering and Design

CHAOTIC BEHAVIOR AND HALO DEVELOPMENT IN THE TRANSVERSE DYNAMICS OF HEAVY ION BEAMS

Chiping Chen
Plasma Fusion Center
Massachusetts Institute of Technology
Cambridge, Massachusetts 02139

Qian Qian and Ronald C. Davidson
Plasma Physics Laboratory
Princeton University
Princeton, New Jersey 08543

ABSTRACT

This paper reviews results obtained from recent analytical and numerical investigations of chaotic behavior and halo development induced by charge density inhomogeneities in the transverse dynamics of heavy ion beams. In particular, a test-particle model is used to investigate the charged-particle dynamics in an intense, matched, heavy ion beam with nonuniform density profile propagating through an alternating-gradient quadrupole magnetic field in the space-charge-dominated regime. It is shown that self-field nonlinearities due to transverse nonuniformities in the beam density not only can result in chaotic ion motion but also can cause halo formation. For heavy ion fusion applications, these results indicate that accurate density profile control is critical in preventing heavy ion beams from developing halos.

I. INTRODUCTION

An important aspect in the design of advanced accelerators and beam transport systems for heavy ion fusion applications [1] is to find optimal operating regimes in which the emittance growth and beam losses are minimized. For ideal beam focusing systems, a primary source of emittance growth is due to the intrinsic beam space-charge effects. Indeed, Hofmann, *et al.* [2] have shown that under certain conditions, the Kapchinskij-Vladimirskij (K-V) beam distribution [3, 4], the only known collisionless equilibrium for periodically focused intense ion beams, exhibits space-charge-induced instabilities, resulting in emittance growth and possible beam losses.

Recent self-consistent simulation studies [5, 6] of intense ion beam propagation indicate that mismatched beams develop halos, and that the halo ions can contribute to the emittance growth and are most likely to be lost in the beam transport systems. One of the consequences of halo-induced beam losses is the production of residual radioactivity in the system, so that continuous operation becomes problematic. Several mechanisms for halo development have been proposed [7]. However, none of these models has been fully validated, both because the presence of numerical noise in particle-in-cell (PIC) simulations makes a direct verification of halo formation extremely difficult, and also because it is difficult in experiments to single out individual effects that may produce beam halos.

In this paper, we review results obtained from recent analytical and numerical investigations [8, 9] of chaotic behavior and halo development induced by charge density inhomogeneities in the transverse dynamics of heavy ion beams. In particular, use is made of a test-particle model to investigate the dynamics of root-mean-squared (rms) matched, intense heavy ion beams propagating through an alternating-gradient quadrupole magnetic field. The elliptical cross-section of the beam is incorporated in the present analysis, assuming that the beam has a parabolic density profile transverse to the propagation di-

rection. A distribution function that is consistent with the assumed density profile is used to specify the initial conditions for the test particles. It is shown that self-field nonlinearities due to the transverse nonuniformity in the beam density profile not only can induce chaotic ion motion [10] but also can lead to halo formation. Because rms beam matching, which does not guarantee necessarily beam matching except for the (ideal) K-V beam equilibrium, is widely utilized in the design of accelerator and beam transport systems, the halo formation mechanism reported in this paper is of particular importance not only in the development of intense heavy ion accelerators for fusion applications, but also in the development of intense proton accelerators for applications such as tritium production [11].

II. MODEL AND ASSUMPTIONS

We consider an rms-matched, continuous, intense heavy ion beam propagating in the z -direction through an alternating-gradient quadrupole magnetic field with axial periodicity length S (Fig. 1). In the paraxial approximation, the transverse equations of motion for an individual ion can be expressed as [3]

$$\frac{d^2x}{ds^2} + \kappa_q(s)x + \frac{q}{\gamma_b^3 \beta_b^2 mc^2} \frac{\partial}{\partial x} \phi(x, y, s) = 0, \quad (1)$$

and

$$\frac{d^2y}{ds^2} - \kappa_q(s)y + \frac{q}{\gamma_b^3 \beta_b^2 mc^2} \frac{\partial}{\partial y} \phi(x, y, s) = 0, \quad (2)$$

where $s = \beta_b ct$ is the axial coordinate, the periodic function $\kappa_q(s) = \kappa_q(s + S) = (q/\gamma_b m \beta_b c)(\partial B_x^q/\partial y)_0$ describes the quadrupole focusing field, $\phi(x, y, s)$ and $\beta_b \phi(x, y, s) \vec{e}_z$ are the scalar and vector potentials associated with the space-charge and current of the intense ion beam, q and m are the ion charge and rest mass, respectively, c is the speed of light in *vacuo*, $\beta_b c$ is the average axial beam velocity, and $\gamma_b = (1 - \beta_b^2)^{-1/2}$ is the relativistic mass factor.

To employ the test-particle model, we determine an analytical expression for the scalar potential, assuming that the beam density profile has the parabolic form

$$n_b(x, y, s) = \begin{cases} \hat{n}_b + \delta\hat{n}_b - 2\delta\hat{n}_b(x^2/a^2 + y^2/b^2), & \text{for } x^2/a^2 + y^2/b^2 \leq 1, \\ 0, & \text{otherwise,} \end{cases} \quad (3)$$

as illustrated in Fig. 2. In Eq. (3), $N = \pi ab\hat{n}_b = \int n_b dx dy = \text{const.}$ is the number of ions per unit axial length. The parameter $\delta\hat{n}_b = \delta N/\pi ab$ is a measure of the nonuniformity of the beam density, and is allowed to be in the range $0 \leq \delta\hat{n}_b \leq \hat{n}_b$. The periodic outermost beam envelope functions, $a(s) = a(s + S)$ and $b(s) = b(s + S)$, are determined from Eqs. (6) and (7). From the equilibrium Poisson equation, the scalar potential is given by [8, 9]

$$\phi(x, y, s) = -\pi q ab \left[\int_0^\xi \frac{\hat{n}_b dt}{[(a^2 + t)(b^2 + t)]^{1/2}} + \int_\xi^\infty \frac{dt}{[(a^2 + t)(b^2 + t)]^{1/2}} \int_0^T n_b(T') dT' \right], \quad (4)$$

where $n_b(T) = \hat{n}_b + \delta\hat{n}_b - 2\delta\hat{n}_b T$ for $0 \leq T \leq 1$, and $n_b(T) = 0$ otherwise, and the variable T is defined by

$$T(x, y, t) = \frac{x^2}{a^2 + t} + \frac{y^2}{b^2 + t}. \quad (5)$$

Here, the function $\xi = \xi(x, y)$ is defined by $T(x, y, \xi) = 1$ for any point outside the beam, and by $\xi = 0$ for any point inside the beam. After a straightforward but lengthy calculation, a closed analytical expression for $\phi(x, y, s)$ can be obtained for the assumed parabolic density profile [9].

Making use of the rms beam envelope equations obtained by Sacherer [12], it can be shown that the periodic envelope functions for the rms matched beam, $a(s) = a(s + S)$ and $b(s) = b(s + S)$, solve the coupled differential equations,

$$\frac{d^2 a}{ds^2} + \kappa_q(s)a - \frac{2gK}{a+b} - \frac{g^2 \epsilon_x^2}{a^3} = 0, \quad (6)$$

$$\frac{d^2 b}{ds^2} - \kappa_q(s)b - \frac{2gK}{a+b} - \frac{g^2 \epsilon_y^2}{b^3} = 0, \quad (7)$$

where $K = 2q^2 N / \gamma_b^3 \beta_b^2 m c^2$ is the normalized beam perveance, $g = (1 - \delta N / 3N)^{-1}$ is the density shape factor, and ε_x and ε_y are the unnormalized rms emittances in the x - and y -directions, respectively. Both ε_x and ε_y are taken to be constant because the present test-particle model is aimed at the *onset* of halo formation, where the rms properties of the beam are not expected to vary appreciably.

For a quadrupole focusing channel with the step-function lattice illustrated in Fig. 3, the periodic envelope functions $a(s)$ and $b(s)$ are obtained numerically from Eqs. (6) and (7) and are plotted in terms of the rescaled quantities $a(s)/\sqrt{g\varepsilon_x S}$ and $b(s)/\sqrt{g\varepsilon_y S}$ in Fig. 4. The choice of system parameters in Fig. 4 corresponds to: $\eta = 0.5$, $\sigma_0 = 75^\circ$, $\delta N / N = 0.1$ ($g \cong 1.03$), $SK/\varepsilon_x = 10.0$, and $\varepsilon_x = \varepsilon_y$. Here, the parameter η is the filling factor for the step-function lattice [13]; and $\sigma_0^2 = S \int_0^S ds [f_{s_0}^s ds \kappa_q(s)]^2$ is a measure of the average focusing field strength-squared, and is approximately equal to the vacuum phase advance-squared [13]. For the case shown in Fig. 4, the space-charge-depressed phase advances, as defined by $\sigma_x = g\varepsilon_x \int_0^S ds / a^2(s)$ and $\sigma_y = g\varepsilon_y \int_0^S ds / b^2(s)$, are calculated to be $\sigma_x = 12.89^\circ$ and $\sigma_y = 12.89^\circ$.

It is important to specify initial conditions for the test-particle motion that are consistent with the density profile assumed in Eq. (3). This is accomplished by the particular choice of initial distribution function at $s = s_0$,

$$f(x, y, x', y', s_0) = \frac{N - \delta N}{\pi^2 g^2 \varepsilon_x \varepsilon_y} \delta(W - 1) + \frac{2\delta N}{\pi^2 g^2 \varepsilon_x \varepsilon_y} H(W). \quad (8)$$

In Eq. (8), $\delta N \equiv \pi a b \delta \hat{n}_b$, the ‘prime’ denotes the derivative with respect to s , $\delta(x)$ is the Dirac δ -function, $H(x)$ is the function defined by $H(x) = +1$ for $0 \leq x \leq 1$, and $H(x) = 0$, otherwise, and W is the variable defined by

$$W = \frac{x^2}{a^2} + \frac{1}{g^2 \varepsilon_x^2} (ax' - xa')^2 + \frac{y^2}{b^2} + \frac{1}{g^2 \varepsilon_y^2} (by' - yb')^2. \quad (9)$$

Here, a , a' , b , b' denote the ‘initial’ values at $s = s_0$. It is readily verified that $n_b(x, y, s_0) = \int f dx' dy'$ indeed yields the parabolic density profile in Eq. (3), and that

$\pi g \varepsilon_x$ and $\pi g \varepsilon_y$ are the maximum initial areas occupied by the beam particles in the phase planes (x, x') and (y, y') , respectively.

The dynamical equations (1) and (2) together with Eqs. (3)-(9) completely describe the model and are used subsequently to show halo formation in nonuniform density beams. For $\delta N = 0$ (i.e., for $g = 1$), the beam density is uniform and the self fields have a linear dependence on x and y within the ellipse defined by $(x/a)^2 + (y/b)^2 = 1$, corresponding to the K-V beam equilibrium. In this case, Eqs. (1) and (2) reduce to coupled (linear) Hill's equations, and the ion orbits are confined within the beam envelope, provided the latter is stable.

For a *nonuniform* beam with $\delta N > 0$ (i.e., with $g > 1$), however, Eqs. (1) and (2) are *nonlinear* due to the nonlinearities in the self-field forces. The ion orbits are non-integrable and can become chaotic, as shown previously in the constant-radius-envelope approximation [10]. This is also true for periodically varying envelope functions. Because Eqs. (1) and (2) are nonintegrable, numerical analyses prove to be more effective than analytical approaches. In the present analysis, both the Adams Predictor-Corrector scheme [14] and the Baker-Campbell-Hausdorff scheme [15] (which is an explicit fourth-order symplectic scheme) are used to integrate numerically Eqs. (1) and (2), where the periodic functions $a(s)$ and $b(s)$ are obtained numerically from the envelope equations (6) and (7). Using the analytical expression for the scalar potential ϕ [9], various benchmark studies have been carried out to assure that the computer round-off errors are negligibly small and do not affect the results presented in the remainder of this article.

III. PHASE SPACE STRUCTURE FOR THE ONE-DIMENSIONAL PARTICLE MOTION

It can be shown [9] that any particles initially loaded in the phase plane (x, x') with

$(y, y') = (0, 0)$ will remain in this phase plane, and are described by the Hamiltonian

$$H = \frac{1}{2} \left(\frac{dx}{ds} \right)^2 + \frac{1}{2} \kappa_q(s) x^2 + \frac{q}{\gamma_b^3 \beta_b^2 m c^2} \tilde{\phi}(x, s), \quad (10)$$

where the potential $\tilde{\phi}(x, s)$ is given by

$$\tilde{\phi}(x, s) = \phi(x, y = 0, s). \quad (11)$$

Therefore, it is fruitful to examine the phase space structure described by Eq. (10) in this section.

Figure 5 shows the Poincaré surface-of-section plots in the phase plane (x, x') for propagation over 400 lattice periods, as described by the decoupled Hamiltonian defined in Eq. (10). The system parameters are chosen to be $\eta = 0.5$, $\sigma_0 = 75^\circ$, $KS/\varepsilon_x = 10.0$, and $\varepsilon_x = \varepsilon_y$. Following the standard procedure of generating Poincaré surface-of-section plots [15], a collection of 41 test particles is loaded initially at $s = s_0 = 0$ with x/a ranging from -2.0 to 2.0 along the $x' = 0$ axis in both Fig. 5(a) and 5(b). Particle trajectories are followed by numerically integrating the Hamilton equations of motion derived from Eq. (10). The particle locations in the phase space (x, x') are plotted at the end of each lattice period, i.e., at $s = 0, S, 2S, \dots, 400S$.

Shown in Fig. 5(a) is the case of a uniform density profile with $\delta N = 0$. In Fig. 5(a), two distinct regions are evident in the phase space (x, x') – one regular region and one chaotic region. The elliptical invariant curves inside the regular region are described by

$$\frac{x^2}{a^2} + \frac{a^2 x'^2}{\varepsilon_x^2} = r^2, \quad (0 \leq r \leq 1), \quad (12)$$

where ε_x is the beam emittance in the x -direction, and the boundary of the regular region is determined by $r = 1$. Because $a' = da/ds = 0$ at $s = nS$, where $n = 0, 1, 2, \dots$, as shown in Fig. 4, equation (12) is equivalent to

$$W_x(s) = \frac{x^2}{a^2} + \frac{1}{g^2 \varepsilon_x^2} (ax' - xa')^2 = \text{const.}, \quad (s = 0, S, 2S, \dots), \quad (13)$$

where $g = 1$ for the uniform density profile. Making use of the invariants $y = 0 = y'$, the constraint in Eq. (13) is consistent with the expected result of $W(s) = \text{const.} \leq 1$ for a K-V beam equilibrium. Here, $W(s)$ is defined in Eq. (9). Note that there is a large chaotic region outside the beam with $W_x > 1$, which is due to the nonlinearity of the self fields outside the beam [16]. The chaotic region is bounded between $W_x = 1$ and an outer Kolmogorov-Arnold-Moser (KAM) surface [15] which is the invariant curve intersecting the x -axis at $x \cong \pm 1.5$ in Fig. 5(a).

The case of a nonuniform density beam is shown in Fig. 5(b) for $\delta N/N = 0.1$. In contrast to the uniform density case illustrated in Fig. 5(a), there is an (unstable) X -point at the origin $(x, x') = (0, 0)$, and two stable points at $(x, x') = (\pm 0.8, 0)$ in Fig. 5(b). Despite existence of the X -point, particles near the origin are well confined and have regular orbits. However, because of the X -point, the chaotic region has engulfed part of the regular region near the origin and becomes accessible to particles that are initially located on the ellipse $W_x(0) \lesssim 1$ and that would otherwise be well confined inside a uniform density beam. It is the loss of the regular phase space region with $W_x(0) \lesssim 1$ that causes a nonuniform density beam to develop a halo on the order of a few lattice periods.

With regard to the outer KAM surface, Figs. 5(a) and 5(b) show qualitatively the same structure; that is, the large chaotic region, which corresponds to a halo for the case of a nonuniform density beam, is bounded by an outer KAM surface. For the fully coupled system described by Eqs. (1) and (2), this implies that the halo is bounded radially on a time scale which is much shorter than that of Arnold diffusion [15].

In order to determine the condition for particles to enter the large chaotic region to form a halo for the initial distribution function defined in Eq. (8), the dynamics of particles initially with $W_x(0) \leq 1$ is studied further. The results are presented in Fig. 6. Figure 6(a) shows the Poincaré surface-of-section plot for a class of particles with

$W_x(0) = 1$ at $s = 0$. The initial conditions in the phase space (x, x') are indicated by the bold dots, and their subsequent trajectories are followed by numerically integrating the Hamiltonian in Eq. (10) for propagation over 400 lattice periods ($s = 400S$). There are two classes of particles in Fig. 6(a). Particles with large initial displacement (i.e., in the range $0.5 \leq |x/a| \leq 1$) are located inside the regular region and their orbits are regular. However, particles with small initial displacement (i.e., with $|x/a| < 0.5$) enter the chaotic region, becoming halo particles. Since the chaotic region in phase space is connected between $|x/a| < 1$ and $|x/a| > 1$, the chaotic behavior in the particle motion leads to the *rapid* escape of particles from the beam interior. The chaotic particle orbits are bounded by a KAM surface at a large radius outside the beam (i.e., at $|x/a| \cong 1.5$), as shown in Fig. 6(a).

In Fig. 6(b), the Poincaré surface-of-section plot is shown for particles initially loaded on the ellipse $W_x(0) = 0.25$ for system parameters otherwise the same as in Fig. 6(a). Evidently, all particles on the ellipse $W_x(0) = 0.25$ are on invariant curves and are well confined inside the beam. It is found in these numerical studies that for the present system parameters all particles with $W_x(0) \lesssim 0.5$ are located within the regular region, and that particles with $W_x(0) > 0.5$ and small displacement $|x/a| \ll 1$ enter the chaotic region, forming a halo.

IV. NUMERICAL ANALYSIS OF THE TEST PARTICLES

Figure 7 shows the Poincaré map of the trajectories of 100 test ions for the phase plane (x, y) as the test ions pass each lattice period, i.e., at $s = 0, S, 2S, \dots, 400S$. The ions are initially loaded at $s = s_0 = 0$ according to the distribution function in Eq. (8) for the choice of system parameters corresponding to: $\eta = 0.5$, $\sigma_0 = 80^\circ$, $SK/\varepsilon_x = 10.0$, and $\varepsilon_x = \varepsilon_y$. Case (a) corresponds to a uniform-density (K-V) beam with $\delta N = 0$ ($g = 1$), while case (b) corresponds to a nonuniform-density beam with $\delta N/N = 0.1$

($g \cong 1.03$). In Fig. 7(a), all of the ion orbits are enclosed within the elliptical beam boundary, i.e., within the solid circle defined by $(x/a)^2 + (y/b)^2 = 1$, as expected for a K-V beam. In contrast, Fig. 7(b) shows a tenuous halo of ions surrounding a dense core for the case of a nonuniform-density beam. The dense core is indicated by the solid circle $(x/a)^2 + (y/b)^2 = 1$. Figure 7(c) shows the Poincaré surface-of-section in the phase plane (x, y) for a single halo particle for the case shown in Fig. 7(b). The maximum radial excursion of halo particles in Fig. 7 is about two times the maximum envelope radius for the particular set of parameters chosen in the figure.

The dynamics of test particles has been studied numerically over a wide region in the parameter space $(\sigma_x, SK/\varepsilon_x, \delta N/N)$. As in a generic nonintegrable Hamiltonian system, it is found that the phase space structure changes abruptly as the system parameters are varied. Consequently, the halo size (i.e., the maximum radial excursion of halo particles) is also found to exhibit sensitive dependences on the system parameters.

Finally, the transverse energy $W(s)$ is plotted in Fig. 8 as a function of the axial distance s for propagation over 200 lattice periods ($s = 200S$). Here, the solid curve corresponds to a core particle, whereas the dotted curve corresponds to a halo particle. Also shown in Fig. 8 as a bold solid curve is the ensemble average value of $W(s)$ for the 100 test particles followed. The choice of system parameters in Fig. 8 corresponds to: $\eta = 0.5$, $\sigma_0 = 75^\circ$, $SK/\varepsilon_x = 10.0$, $\varepsilon_x = \varepsilon_y$, $\delta N = 0$ for case (a), and $\delta N/N = 0.1$ for cases (b), (c), and (d). While the value of $W(s)$ for the core particle varies moderately within the upper limit $W(s) \lesssim 1$, the value of $W(s)$ for the halo particle varies by a large amount for propagation over 200 lattice periods, with the peak value of $W(s)$ close to four times the initial value. More importantly, the halo particles can gain energy and escape from the beam interior in a few lattice periods as shown in Fig. 8, which is consistent with the results presented in Sec. III. Moreover, the value of the transverse energy $W(s)$ averaged over 100 test particles increases by less than 10% within the first 100 lattice

periods. Since the rms emittance of the beam is a measure of the ensemble average of the transverse energy of the beam particles, this result is consistent with the assumption in the present test-particle model that the beam emittance is approximately constant, although a (slow) systematic increase is evident from Fig. 8.

V. CONCLUSION

To summarize, we have shown using a test-particle model that nonlinearities in the self fields not only can result in chaotic ion motion but also can cause a halo to develop for an intense heavy ion beam propagating through an alternating-gradient quadrupole magnetic field. This is found to be true even when the beam is *matched* in the rms sense in the space-charge-dominated regime which is of considerable practical importance in the design of advanced accelerators. The importance of this mechanism for halo formation, which has long been overlooked, is further elucidated by the fact that the chaotic particle trajectories and the escape of the halo particles from inside the beam are due totally to the nonuniformity in the beam density profile in the present model. For heavy ion fusion applications, these results indicate that accurate density profile control is critical in preventing heavy ion beams from developing halos.

Self-consistent computer simulation studies of the halo mechanism presented in this paper are in progress. The results will be presented in a future publication.

VI. ACKNOWLEDGMENTS

The authors would express their special thanks to Dr. Robert D. Ryne who provided valuable assistance in the numerical computations. This work was supported in part by U.S. Department of Energy Contract No. DE-AC02-76-CHO-3073 and in part by the Office of Naval Research.

References

- [1] R.W. Müller, in *Nuclear Fusion by Inertial Confinement: A Comprehensive Treatise*, edited by G. Velarde, Y. Ronen, and J.M. Martinez-Val (CRC Press, Boca Raton, FL, 1993), p. 437.
- [2] I. Hofmann, L.J. Laslett, L. Smith, and I. Haber, *Part. Accel.* **13**, 145 (1983).
- [3] R.C. Davidson, *Physics of Nonneutral Plasmas* (Addison-Wesley, Reading, MA, 1990), Chapter 10.
- [4] I.M. Kapchinskij and V.V. Vladimirskij, *Proc. Int. Conf. on High Energy Accelerators* (CERN, Geneva, 1959), p. 274.
- [5] A. Cucchetti, M. Reiser, and T. Wangler, *Proc. 1991 Part. Accel. Conf. (IEEE Service Center, Piscataway, New Jersey, 1991)*, Vol. 1, 252.
- [6] C. Chen and R.A. Jameson, *Phys. Rev.* **E52**, 3074 (1995).
- [7] R.L. Gluckstern, *Phys. Rev. Lett.* **73**, 1247 (1994), and references therein.
- [8] Q. Qian, R.C. Davidson, and C. Chen, *Phys. Rev.* **E51**, 5216 (1995).
- [9] Q. Qian, R.C. Davidson, and C. Chen, *Phys. Plasmas* **2**, 2674 (1995).
- [10] Q. Qian, R.C. Davidson, and C. Chen, *Phys. Plasmas* **1**, 1328 (1994).
- [11] R.A. Jameson, in *Advanced Accelerator Concepts*, edited by J.S. Wurtele, American Institute of Physics Conference Proceedings **279**, 969 (1993).
- [12] F.J. Sacherer, *IEEE Trans. Nucl. Sci.* **NS-18**, 1105 (1971).
- [13] R.C. Davidson and Q. Qian, *Phys. Plasmas* **1**, 3104 (1994).

- [14] E. Isaacson and H.B. Keller, *Analysis of Numerical Methods* (John Wiley & Sons, New York 1966).
- [15] A.J. Lichtenberg and M.A. Lieberman, *Regular and Chaotic Dynamics*, 2nd Edition (Springer-Verlag, New York, 1992).
- [16] J.M. Lagniel, Nucl. Instrum. Methods Phys. Res. **A345**, 1516 (1994).

FIGURE CAPTIONS

- Fig. 1 Schematic of intense heavy ion beam propagation through an alternating-gradient quadrupole magnetic field.
- Fig. 2 (a) Elliptical cross-section of the beam, and (b) beam density profile described by Eq. (3).
- Fig. 3 Lattice function $\kappa_q(s)$ for an alternating-gradient quadrupole magnetic field with periodic step-function profile and filling factor η .
- Fig. 4 Nonlinear periodic envelope functions $a(s)$ and $b(s)$ obtained numerically from Eqs. (6) and (7) for $\eta = 0.5$, $\sigma_0 = 75^\circ$, $\delta N/N = 0.1$ ($g \cong 1.03$), $SK/\varepsilon_x = 10.0$, and $\varepsilon_x = \varepsilon_y$. Here, $a(s)$ and $b(s)$ are plotted in terms of rescaled quantities $a(s)/\sqrt{g\varepsilon_x S}$ and $b(s)/\sqrt{g\varepsilon_y S}$.
- Fig. 5 The Poincaré surface-of-section of the decoupled Hamiltonian in Eq. (10) in the phase plane (x, x') . The two cases corresponding to (a) uniform density profile with $\delta N = 0$, and (b) nonuniform density profile with $\delta N/N = 0.1$. The system parameters are given by $\eta = 0.5$, $\sigma_0 = 75^\circ$, $KS/\varepsilon_x = 10.0$, and $\varepsilon_x = \varepsilon_y$.
- Fig. 6 The Poincaré surface-of-section plots in the phase plane (x, x') for particles initially with $W_x(0) \leq 1$. The two cases correspond to (a) $W_x(0) = 1$, and (b) $W_x(0) = 0.25$. The bold dots indicate the initial conditions. The system parameters are the same as the case shown in Fig. 5(b).
- Fig. 7 Poincaré surface-of-section plots for the trajectories of 100 test ions obtained numerically from Eqs. (1) and (2) for propagation over 400 lattice periods. The test ions are loaded initially at $s = s_0 = 0$ according to the distribution function in Eq. (8). The two cases correspond to: (a) a uniform-density (K-V) beam with $\delta N = 0$ ($g = 1$), and (b) a parabolic-density beam with $\delta N/N = 0.1$ ($g \cong 1.03$). The system parameters are otherwise the same in both (a) and (b), and are given by $\eta = 0.5$, $\sigma_0 = 80^\circ$, $SK/\varepsilon_x = 10.0$, and $\varepsilon_x = \varepsilon_y$. Shown in (c) is the

Poincaré surface-of-section plot for the trajectory of a single halo test particle for the case presented in (b).

Fig. 8 Plot of the transverse energy function $W(s)$ over 100 lattice periods for the cases of (a) a test particle in uniform density profile (solid curve), (b) a core particle in a nonuniform density profile (dashed curve), (c) a halo particle (dot-dashed curve), and (d) averaged value of 100 test particles distributed initially according to Eq. (8). Here, the choice of system parameters corresponds to: $\eta = 0.5$, $\sigma_0 = 75^\circ$, $SK/\varepsilon_x = 10.0$, $\varepsilon_x = \varepsilon_y$, $\delta N = 0$ for case (a), and $\delta N/N = 0.1$ for cases (b), (c), and (d).

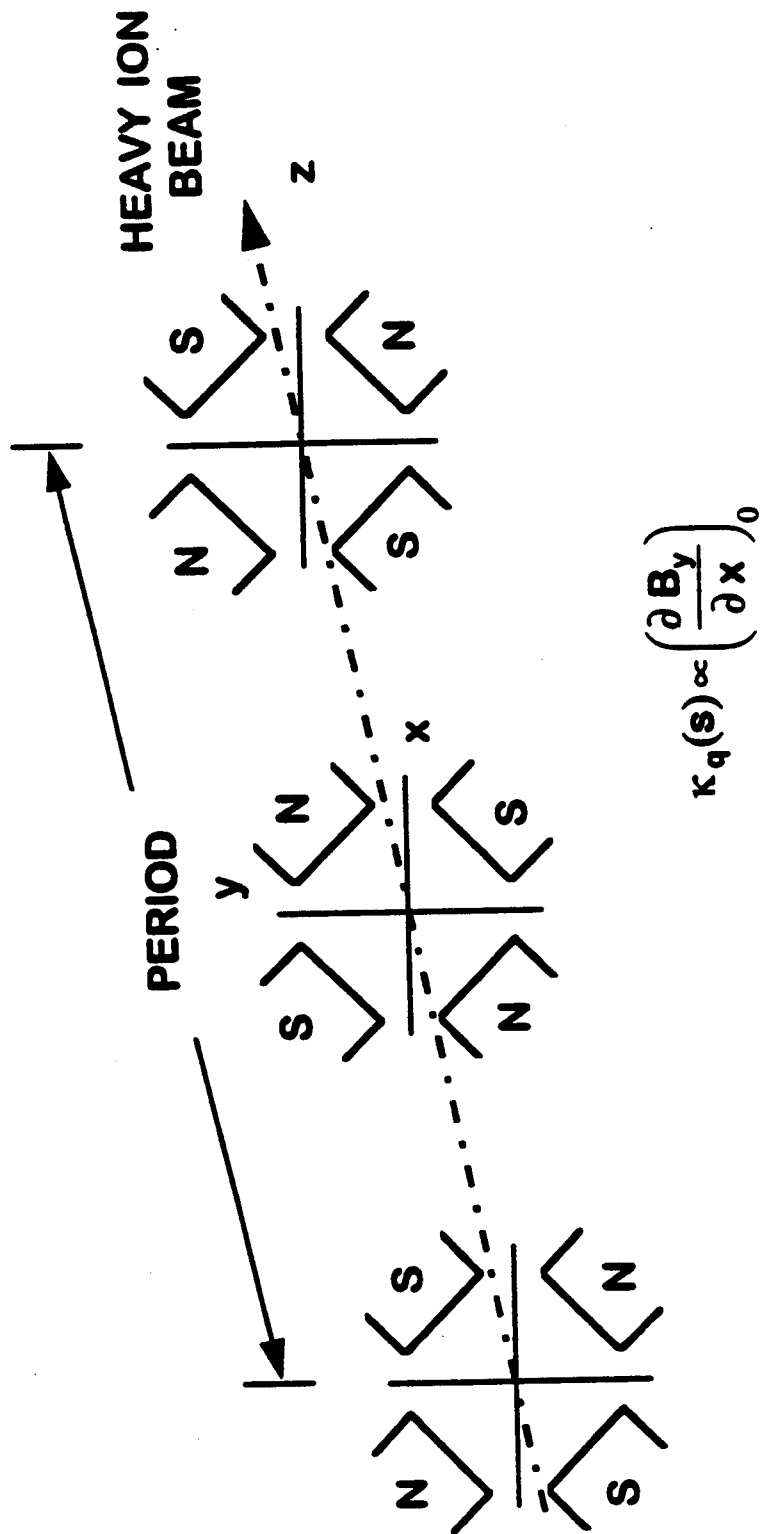


Fig. 1

Chen, Qian & Davidson

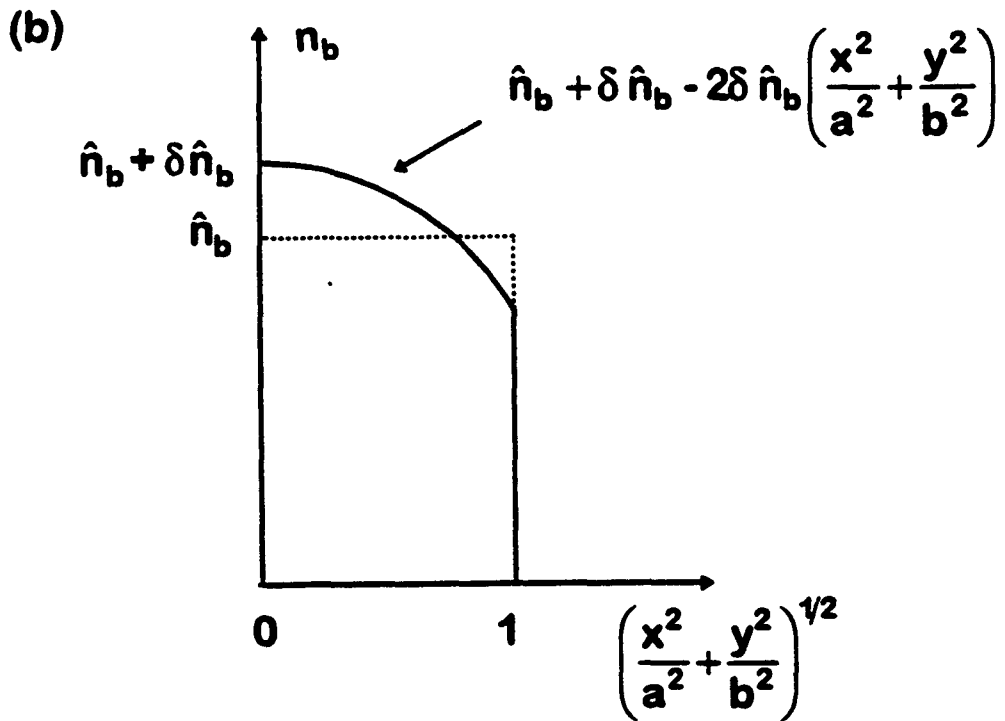
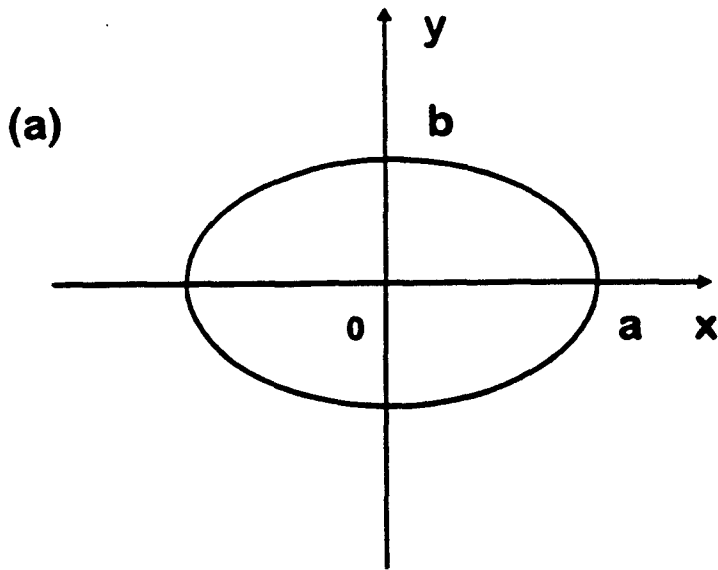


Fig. 2

Chen, Qian & Davidson

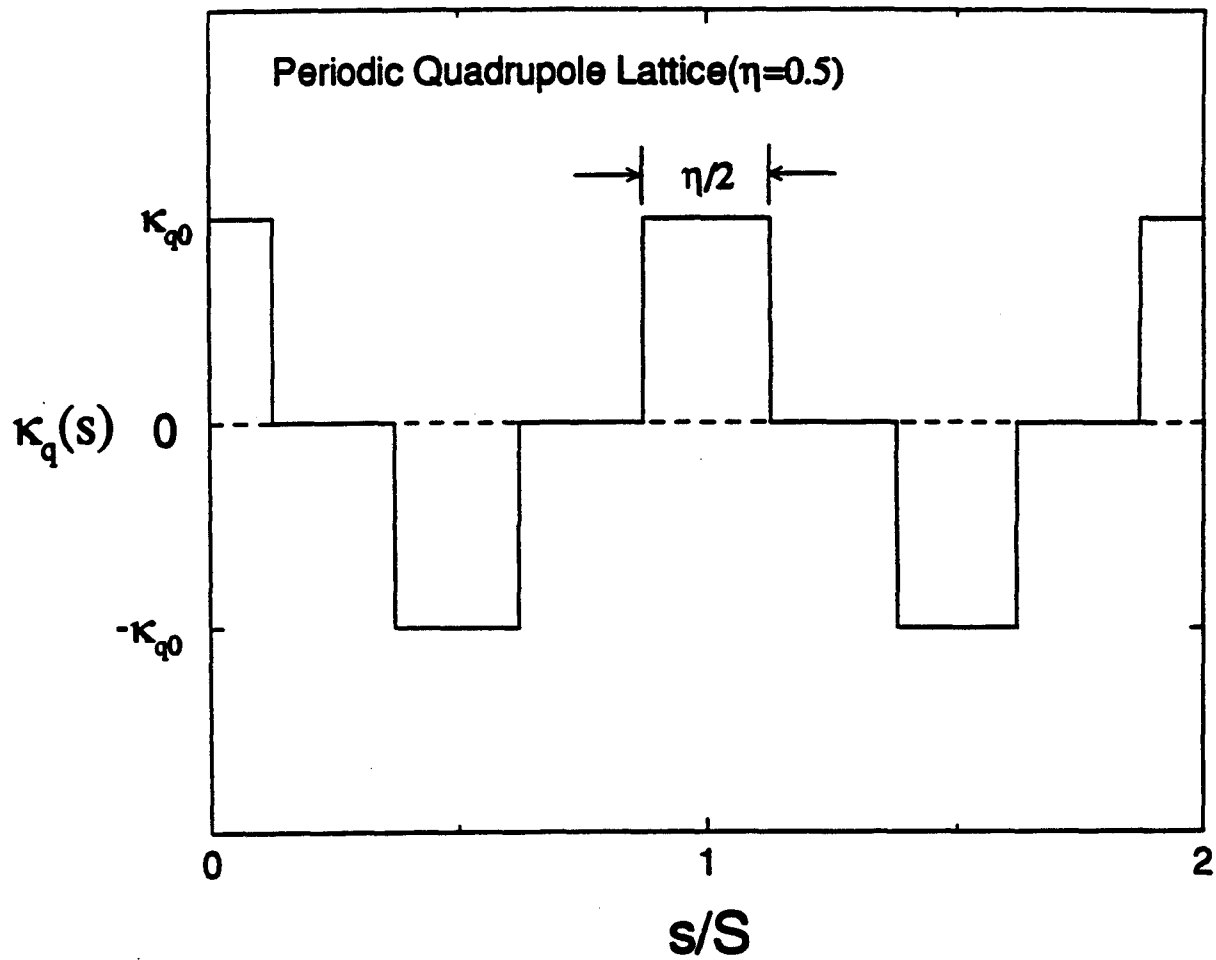


Fig. 3

Chen, Qian & Davidson

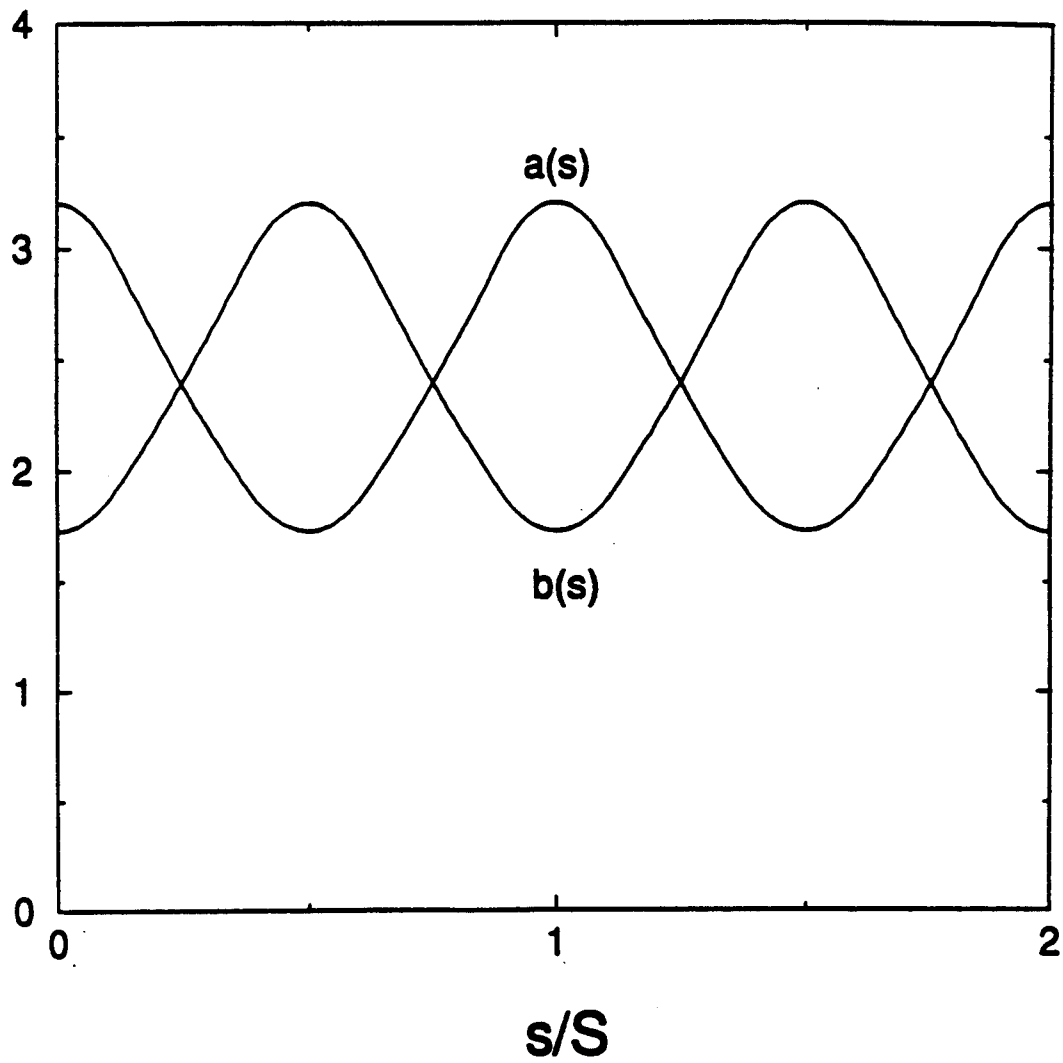


Fig. 4

Chen, Qian & Davidson

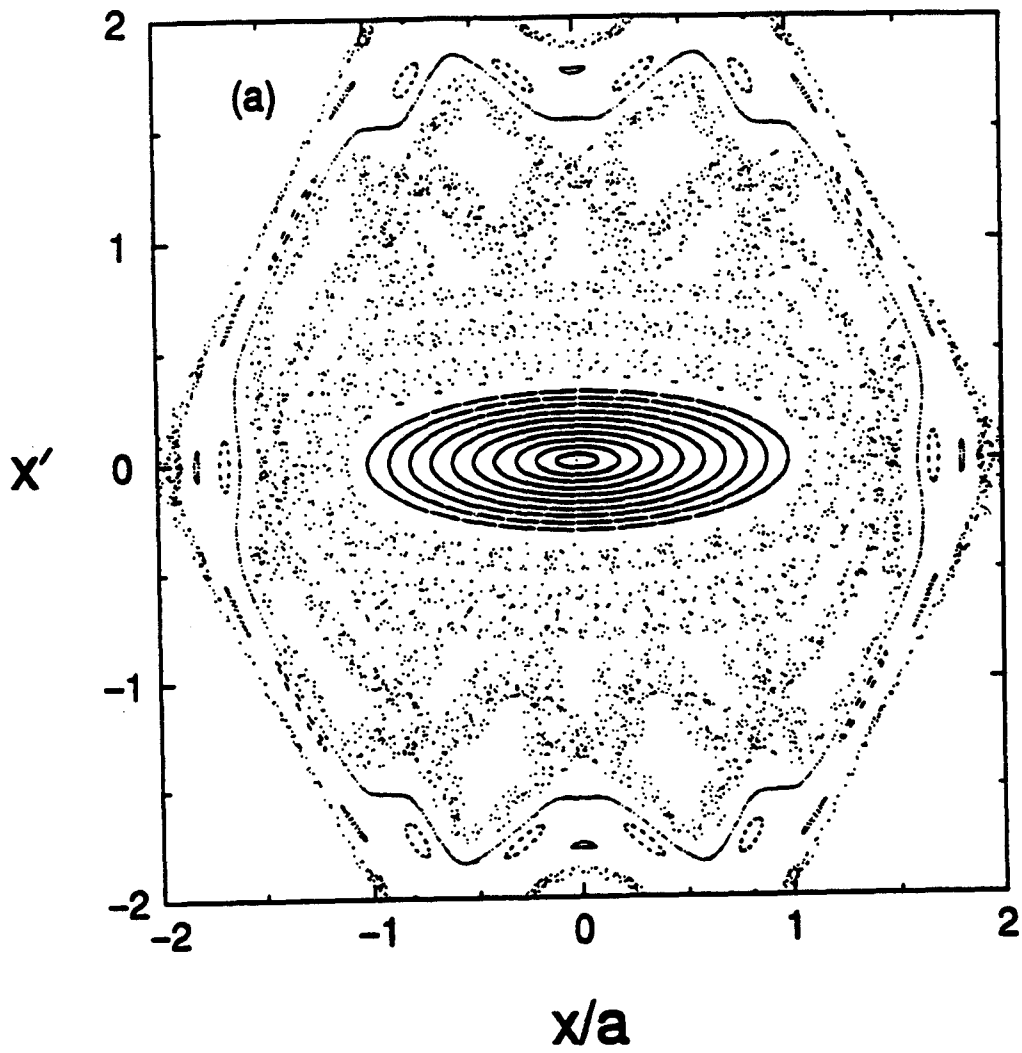


Fig. 5(a)

Chen, Qian & Davidson

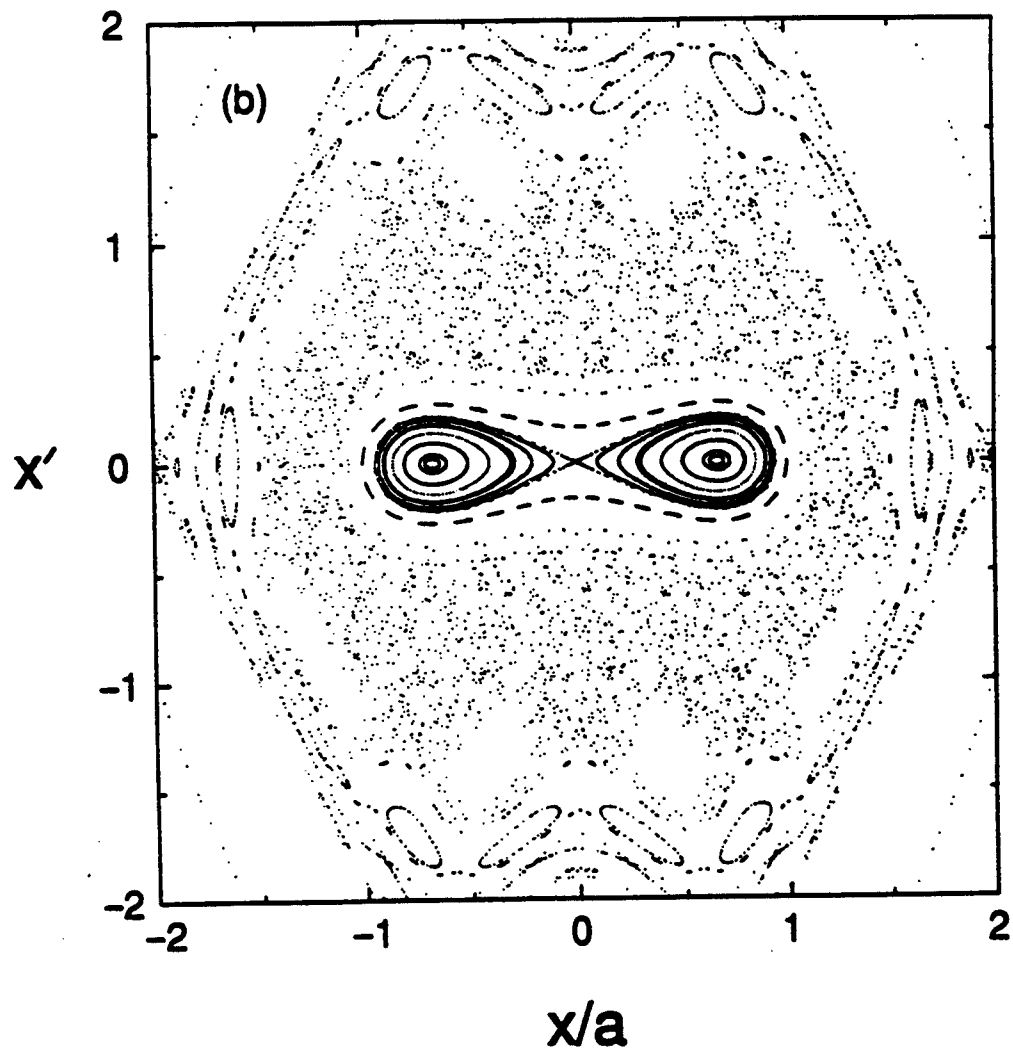


Fig. 5(b)
Chen, Qian & Davidson

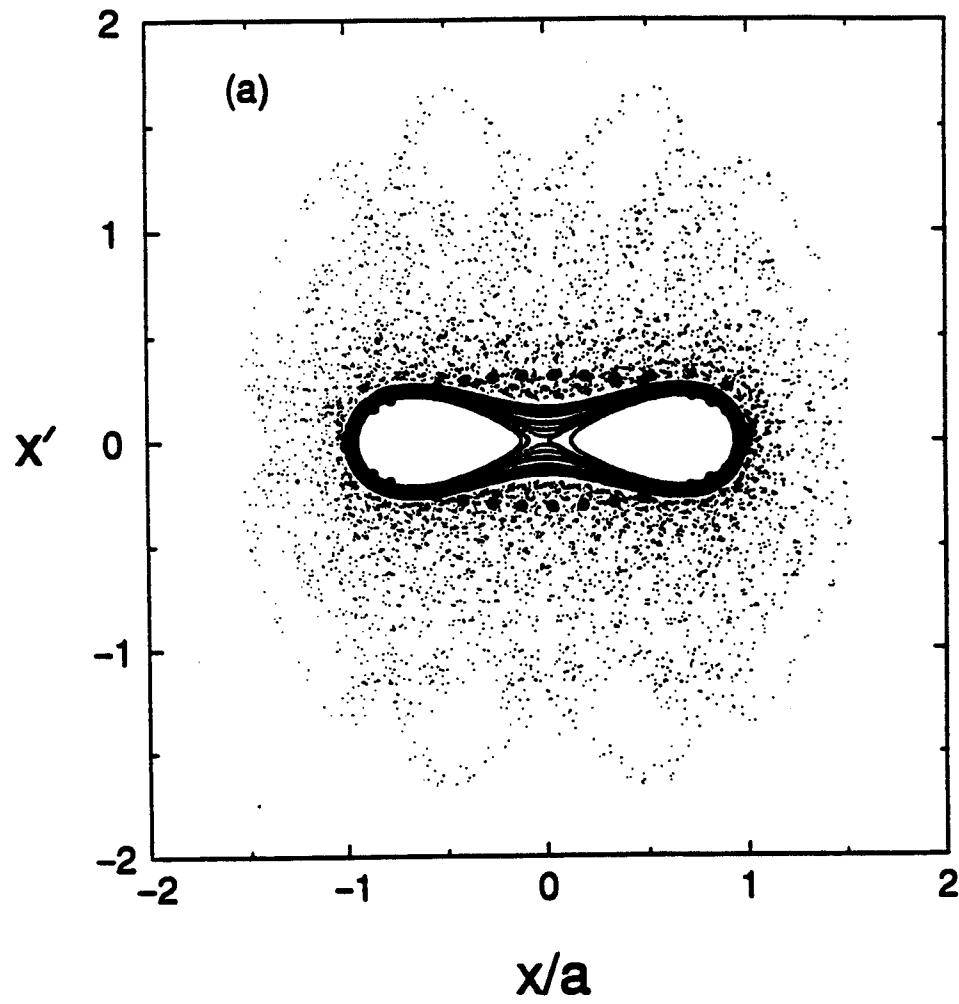


Fig. 6(a)

Chen, Qian & Davidson

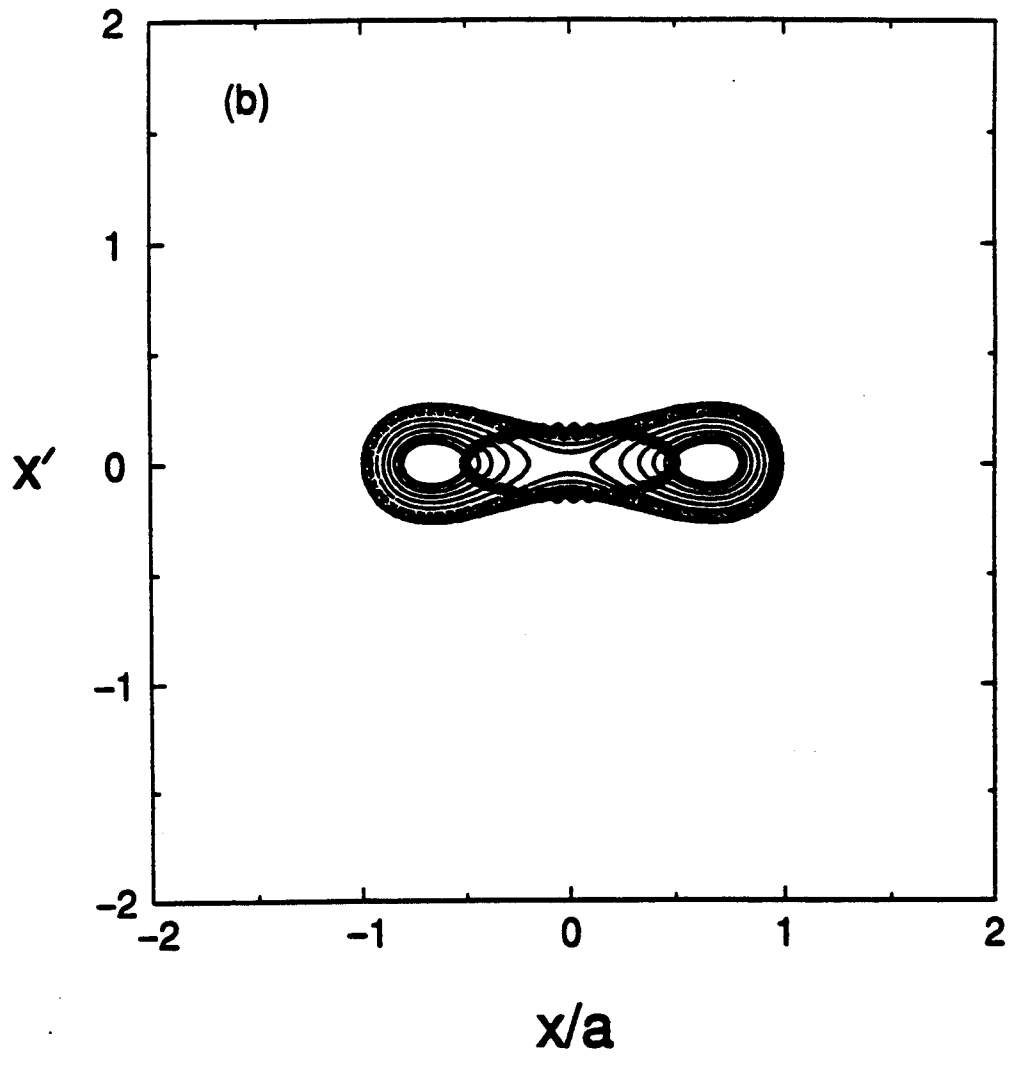


Fig. 6(b)
Chen, Qian & Davidson

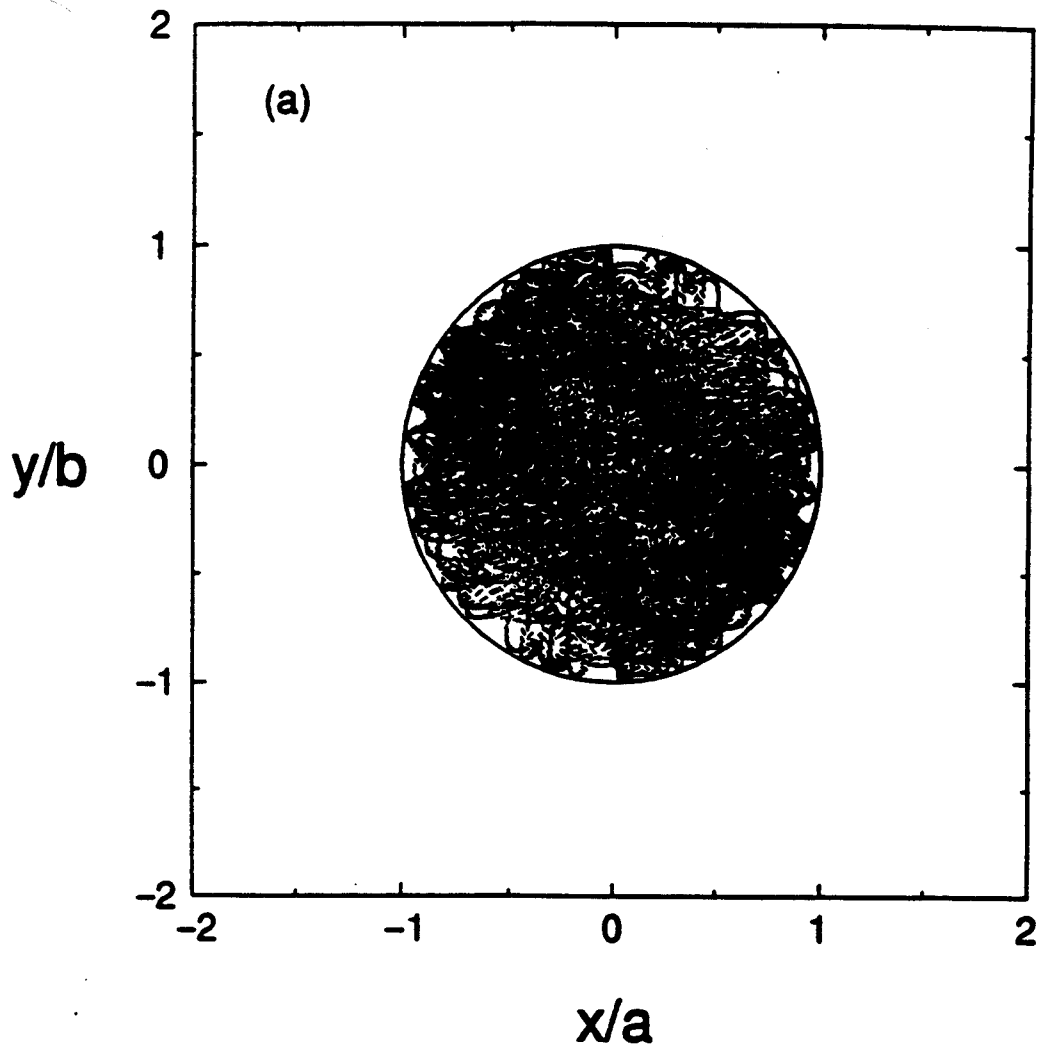


Fig. 7(a)

Chen, Qian & Davidson

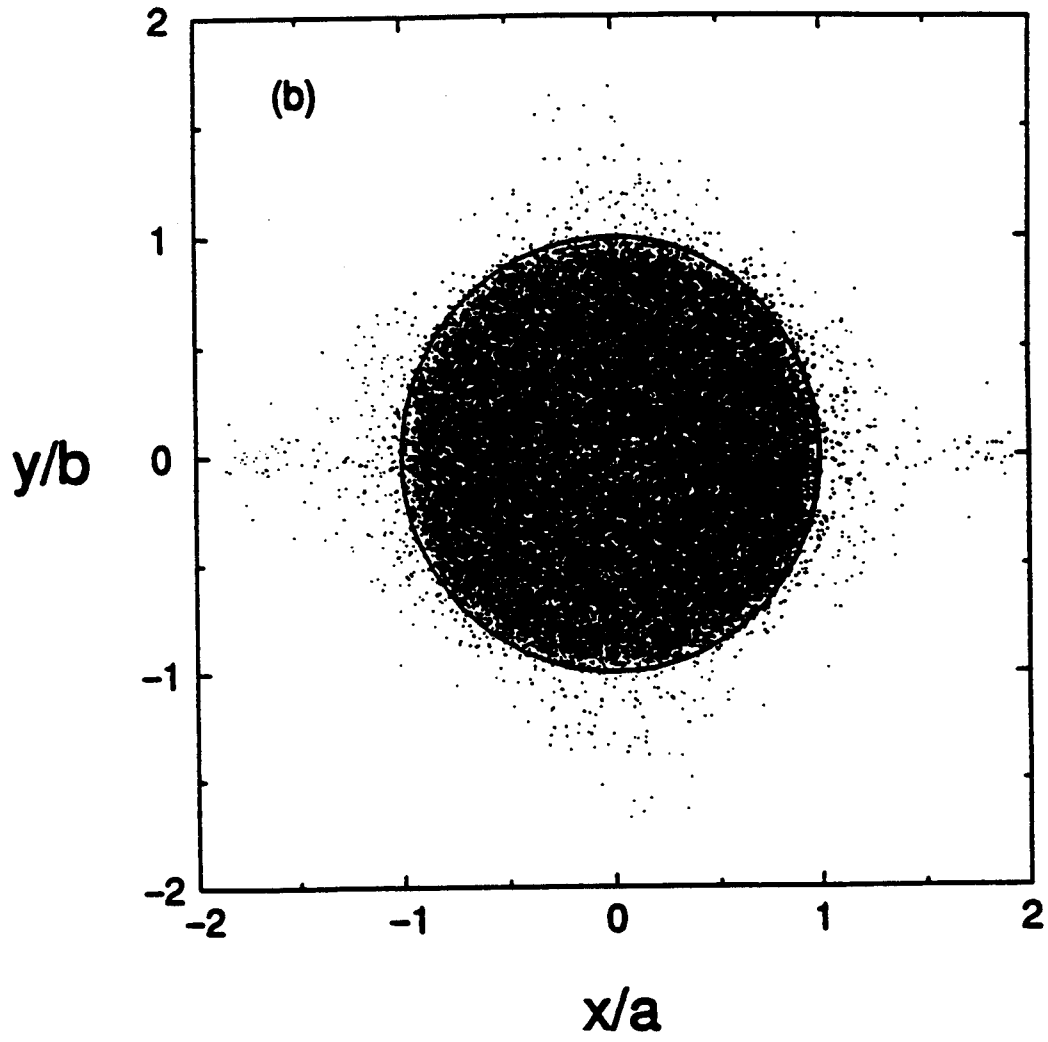


Fig. 7(b)

Chen, Qian & Davidson

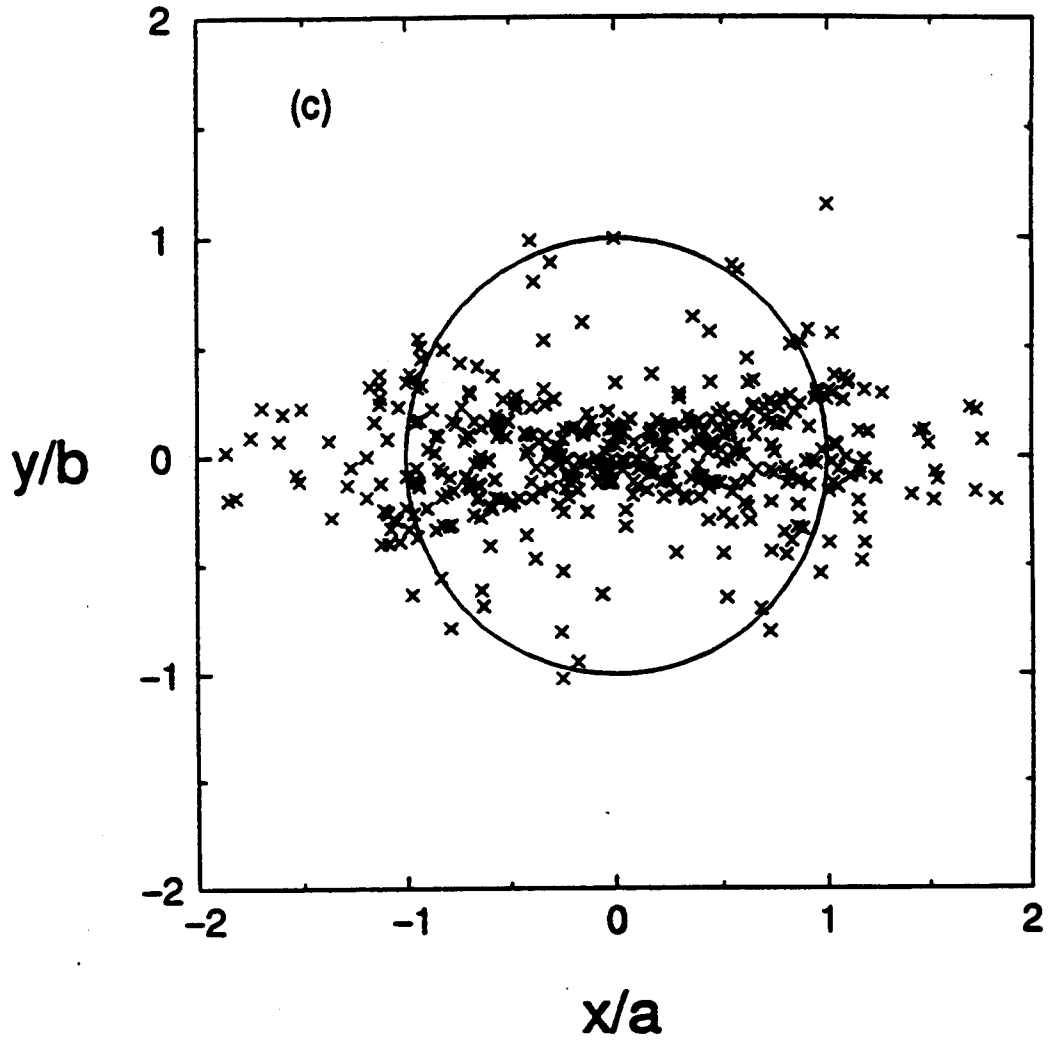


Fig. 7(c)

Chen, Qian & Davidson

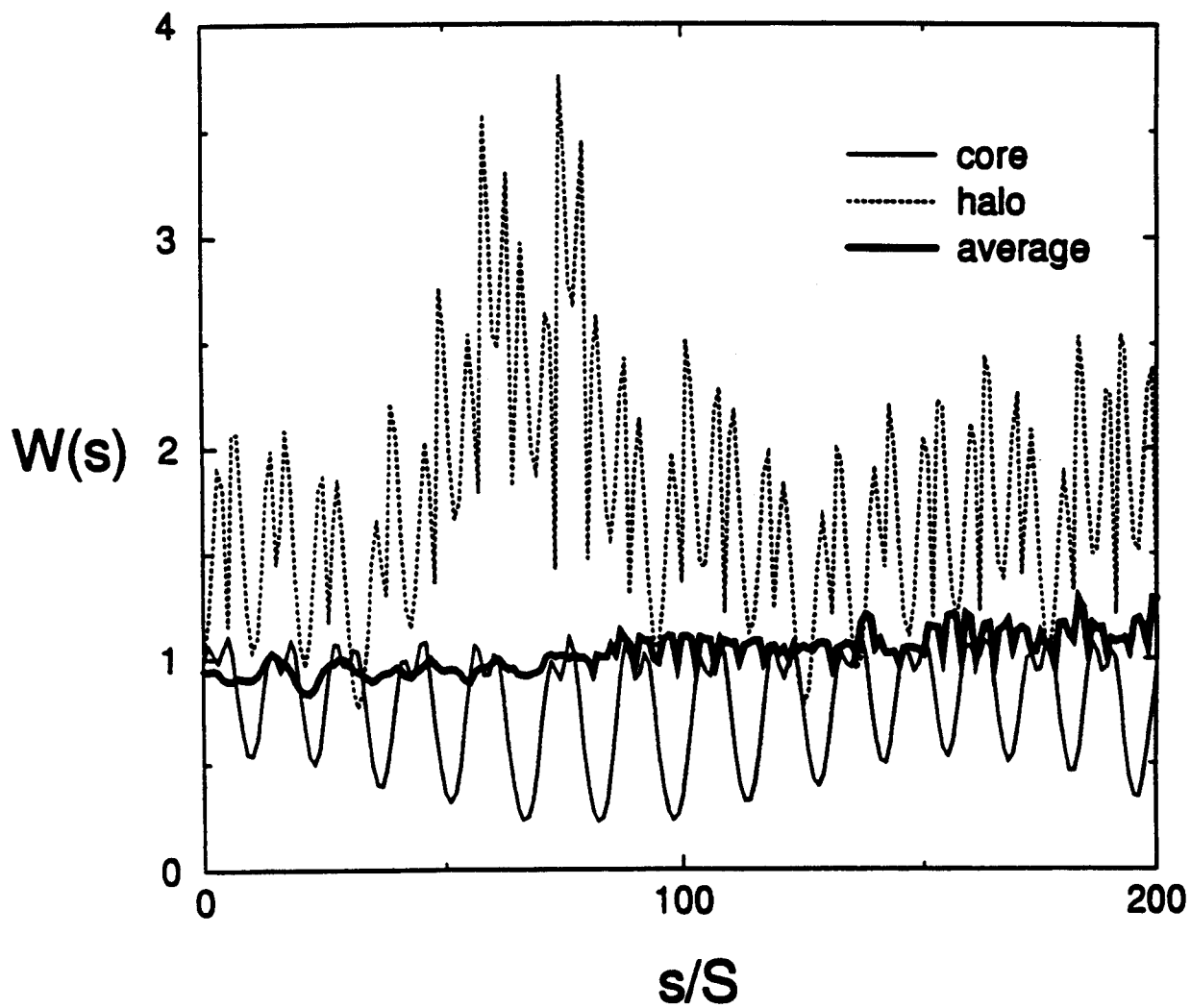


Fig. 8

Chen, Qian & Davidson